A large 3D target with small inner details : A difficult cocktail for imaging purposes without a-priori knowledge on the scatterers geometry,

Christelle Eyraud, Jean-Michel Geffrin, Amelie Litman, Jean Pierre Spinelli

A large 3D target with small inner details: A difficult cocktail for imaging purposes without a-priori knowledge on the scatterers geometry

Christelle Eyraud[1], Jean-Michel Geffrin[1], Amélie Litman[1] and Jean-Pierre Spinelli[1]

To accurately image a complex shape but large 3D target whose scattered field has been measured in an anechoic environment at high frequencies (18 and 20 GHz), we have developed a complete imaging process, combining experimental and numerical works. The adopted strategy exploits the maximum of available information related to the measurements, both in terms of quantity and accuracy without any a-priori knowledge on the scatterer geometry. We first determine the position and then the dimension of the spatial domain which contains the target. This localization is realized directly from the analysis of the spectrum of the measured fields taking into account the random noise disturbing the measurement points. Then, we construct a quantitative permittivity map of this investigation domain thanks to an iterative inversion procedure based on a Bayesian formulation where the spatial diversity of the real random noise is adequately exploited. By following this strategy, we have been able to quantitatively retrieve the target both in terms of dimension, shape and electromagnetic properties, even with a very limited number of measurement points and for a single polarization case. With such a process, even spheres with a diameter equal to $\lambda/3$ are correctly reconstructed at 20 GHz.

1. Introduction

As the physical features of an unknown target are contained in its scattered field, it is possible in theory to retrieve these characteristics thanks to the resolution of an inverse scattering problem. In practice, there exists some difficulties in particular when dealing with measurements. Indeed, as the scattered field can not be measured on an entire closed surface englobing the target, the data are truncated [*Bucci et al.*, 1997], [*Snieder*, 1999]. The measurements are also inevitably disturbed by some noise, moreover this noise a-priori does not follow an uniform distribution [*Geffrin et al.*, 2009].

Recent works in microwave imaging, in particular for buried targets reconstructions, are concerned with the developpement of fast linear algorithms allowing the detection and the localization of the scatterers (see [*Soldovieri*, 2010], [*Litman et al.*, 2010], [*Soldovieri at al.*, 2011] for example). These methods which present a low computational time and a relatively low memory requirement allow exploring large spatial regions. Unfortunately, except for scatterers with small dimensions and/or with low contrasts, these procedures do not lead to quantitative reconstructions.

A complete non-linear formulation is therefore necessary to reach such quantitative values. In these cases, global optimizations as [*Garnero et al.*, 1991], [*Zigliavsky*, 1991] should be preferable due to the possible presence of several local minima, but these methods require generally high computational time. Some approaches have also been developed to reduce the non-linearity degrees of the problem [*Brancaccio et al.*, 1995], [*Isernia et al.*, 1997]. Here, we choose to regularize our problem by using available a-priori information related to the effective measurement noise and to the physical properties of the scatterer.

Another difficulty of the quantitative inversion procedures concerns their large memory storage requirement. To overcome this difficulty, the investigation domain is usually reduced to few wavelengths (see [*Semenov et al.*, 2000], [*Abubakar et al.*, 2004], [*de Zaeytijd et al.*, 2009] for example). Indeed, these procedures are performed with an a-priori knowledge on the position and on the dimension of the tar-

[1]Institut Fresnel, Aix-Marseille Universités, Ecole Centrale Marseille, CNRS, Domaine Universitaire de Saint Jérôme, F-13397 Marseille, France

0048-6604/11/$11.00

get. In some cases, this information is provided, as for example in the last 3D database of experimental scattered fields proposed by the Institut Fresnel (*3D Fresnel database*) [*Geffrin et al.*, 2009], [*Litman et al.*, 2009]. Otherwise, these geometrical features must be directly deduced from the measurements. In [*Catapano et al.*, 2009], the authors have employed the Linear Sampling Method to pre-localize the targets. Our approach, detailed here, is to directly exploit the scattered field spectral behavior to estimate the investigation area.

In this paper, we explain the complete imaging strategy that we have constructed in order to retrieve the target's charactheristics directly from the measured scattered fields and without any a-priori geometrical information related to the target in the measurement scene. In a previous study [*Eyraud et al.*, 2011], we have thoroughly investigated the influence of the polarization effects on the quantitative inversion procedure. In that former study, we have used the a-priori knowledge of the position and the dimensions of the target. Herein, we will focus on the retrieval of the quantitative characteristics of the scatterer without any knowledge on its position and on its approximate extent using the most favourable case of polarization.

The adopted strategy is summarized here. First, the measurements are performed and the fields are post-treated for drift correction and calibration, before being inverted. The imaging procedure is then decomposed into two steps. The first step consists in the localization of the target and the estimation of its size by exploiting the spatial spectrum of the scattered field while taking into account the measurement accuracy. In the second step, a quantitative inversion procedure based on a Bayesian approach, which also takes into account the effective measurement noise, produces the permittivity map within the pre-selected investigation zone.

The present paper is organized as follows. In Section 2, the physical characteristics of the target are described. The experimental work is presented in Section 3. In Section 4, the inversion process is detailed step by step and associated results are presented. Concluding remarks follow in Section 5.

2. Target description

In this study, we consider a 3D non-symmetrical target whose internal structure is particularly complicate while its external dimensions are relatively large with respect to the frequency (5.7 wavelengths at 20 GHz) (Figure 1). This object has been realized in the CEntre de THermIque de Lyon (CETHIL) laboratory, Villeurbanne, France in the framework of an on-going collaboration whose goal is to study the interaction of electromagnetic waves with soot particles [*Merchiers et al.*, 2009]. This target is composed

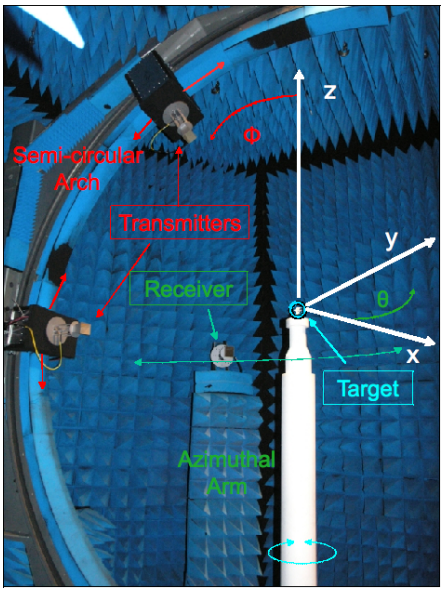

Figure 2. Spherical experimental setup.

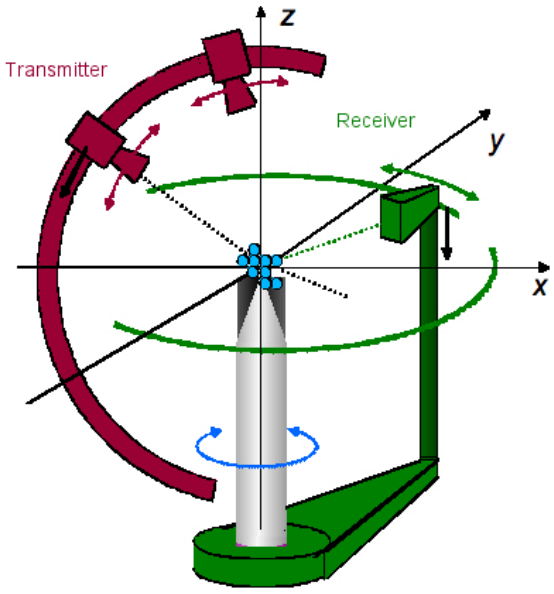

Figure 3. Sketch of the experimental setup.

of 74 small spheres of 5 mm diameter ($\frac{\lambda}{3}$ at 20 GHz).

The permittivity of this target has been measured with the commercial kit *EpsiMu* [*Ba et al.*, 2010] and refined with a minimization procedure, by comparing the measured and the simulated scattered fields of a 50 mm diameter sphere made from the same material and placed within our anechoic chamber. A value of $\varepsilon_r = 2.85 + j0$ was found.

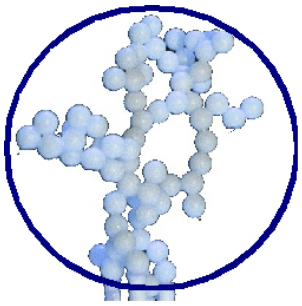

Figure 1. Picture of the 74 spheres aggregate. The diameter of the sphere enclosing the target is equal to 85 mm (5.7λ at 20 GHz).

This target - with its particular geometry - has already been used in former studies and is of interest for analyzing the peformances of our microwave imaging setup, in particular in terms of measurement accuracy and in terms of spatial reconstructed resolution. To assess the first aspect, comparisons between measured scattered fields and simulated ones can be found in [*Merchiers et al.*, 2010] and measurements for direct problem comparisons are also freely available [*Fresnel datasets*, 2010].

3. Measurements

The electromagnetic fields presented herein are measured in the anechoic chamber of the C.C.R.M. (Centre Commun de Ressources en Microondes). The setup is briefly described in the next part and the experimental choices as well as the post-treatments steps are presented in the two following parts.

3.1. Setup description

This facility allows measuring the scattered field on a 2 m sphere enclosing the target of interest. Indeed, the transmitting antenna can move in the xOz plane on a vertical semi-circular arch (ϕ_s angle) while the target can rotate on itself along the z-axis (θ_s angle) (see Figures 2 and 3). This situation is in theory equivalent to a motionless target illuminated by several transmitting antennas positioned on various vertical arches placed all around the object. The receiving antenna moves on a fixed circle in the xOy horizontal plane (θ_r angle). The transmitting antenna and the receiving antenna are linear-polarized high gain pyramidal horns (ARA MWH1826B). The measurements are performed with a Vectorial Network Analyzer (HP 8510 B) used in a measurement configuration with external mixers (HP 85320) and an external synthesizer (HP 83621). The mechanical movements and the VNA are controlled by a monitoring software. Further information can be found in [*Geffrin et al.*, 2005] and [*Sabouroux et al.*, 2005].

3.2. Experimental choices

As this anechoic setup offers various possibilities, we have selected some specific experimental features in order to perform the scattered field measurements in an optimal way.

The first step consists in defining a careful alignment procedure as the challenge is to place this very small target (85 mm) in the middle of our 4000 mm diameter measurement sphere. This was realized with the help of small transparent spheres and the help of a laser beam [*Merchiers et al.*, 2010]. We have then checked that this procedure allows placing the target at the right position. For this specific target, a positioning accuracy (considering the gravity center) better than $\lambda/10$ (1.3 mm) was found in the xOy plane and an accuracy in the order of $\lambda/5$ (2.9 mm) was obtained along the z axis, considering a frequency of 20 GHz [*Eyraud et al.*, 2011]. This very small positioning error is possible thanks to a physical support that bears the aggregate.

As the number of measurement points has a direct consequence in terms of measurement time, it is particularly interesting to accelerate the measurement process. For this, we selected alternatively one of the two antennas on the arch as the transmitting one thanks to a microwave switch (Figure 2). This enables to enrich the number of illumination angles.

A single polarization case is considered herein where, for the transmitting antenna, the electric field is tangential to the vertical arch while, for the receiving antenna, the electric field is oriented along z. This choice corresponds to the best polarization case as shown and explained in [*Eyraud et al.*, 2011]

where the other polarization cases are presented and discussed.

Finally, to get the maximum of information on the target, the measured fields is sampled with a spatial step in accordance with the spatial bandwidth of the scattered field [*Bucci et al.*, 1997] ($\Delta\phi_s = 10°$, $\Delta\theta_r = 5°$ and $\Delta\theta_s = 40°$, this last step is larger than the maximum sampling criterion to keep a reasonable measurement time). Indeed, in a spherical configuration as we are faced with, the scattered field is known to have a limited spectral bandwidth, which enables to determine an optimal field sampling step. This optimum sampling angle depends on the illumination frequency and on the object dimension. For the considered target, at 20 GHz, the number of degrees of freedom of the scattered field [*Bucci et al.*, 1997], i.e., the number of non redundant information which is possible to measure, is equal to 80 000. As the experimental sampling steps are also chosen in accordance to the constraint that the overall measurement time must be reasonable (less than 24h), we are only measuring 6201 transmitting-receiving antenna couples with a minimum of measurement redundancy.

3.3. Post-treatments of the measurements

As these fields are meant for imaging applications, even if they are accurately measured, additional data treatments are required to extract from them the maximum of information related to the target. As a lot of measurements have to be acquired for imaging purposes, drift phenomena (which can be due to wave propagation variations in the cables, to network analyzer drifts and to temperature variations) are particularly dramatic. To compensate for the drift errors, we take advantage of the spatial spectral properties of the scattered field [*Bucci et al.*, 1987]. All the fields are therefore treated with a correcting procedure based on the fact that the spectrum should have a low-pass filter behavior [*Eyraud et al.*, 2006].

As we are interested in performing quantitative reconstructions, a calibration procedure is required to render the scattered field quantitative. The objective is to refer the scattered field measurements from an incident field having an unitary magnitude and a null phase at the center of the setup. As our horn antenna has limited cross-polarization (the difference between the co-polarization and the cross-polarization components is superior to 25 dB), the antenna cross-polarization components are neglected in the calibration. This calibration process is thus realized in three steps. First, one complex-valued coefficient - the same for all the measurements acquired at a given frequency - is determined using a reference target (a metallic sphere in the present case). Both a reference experiment - with a chosen emitting antenna - and a reference calculation - with an incident field as previously defined - are then realized. The calibration coefficient is simply determined by minimizing the discrepancy between the measurement and the calculation [*van den Berg et al.*, 1995; *Eyraud et al.*, 2008]. Second, as two antennas are used successively in place of the transmitting antenna, a supplementary coefficient is added to compensate for the different radiation conditions and their nonidentical feed-lines. Indeed, even if the two antennas are of the same model, some small differences remain. Finally, as the current scattered measurement that we want to calibrate is not realized at the same time as the reference measurement, the drift phenomenon between the two measurements of the incident field is corrected using the associate coefficient defined in [*Geffrin et al.*, 2009].

The measured scattered fields are also disturbed by random noise. This noise is the result of all the different random phenomena provided for example by the source, the mixers, the receiver, ... A previous statistical study [*Geffrin et al.*, 2009] performed on the total field and on the incident field measurements has showed that this random noise is strongly different from one measurement point to another and that its value depends on the measured fields (the incident and the total fields). Indeed, the real part and the imaginary part of the random noise are following two Gaussian laws with standard deviations depending on the magnitude of the incident field, on the magnitude of the total field and on the frequency. To give an idea of these values, at 20 GHz, the mean of the standard deviations (respectively the mean of the scattered field magnitude) is equal to 0.0007 (resp. to 0.033). Important information for this study are that this random noise increases strongly with the frequency. At the high frequencies we are considering herein (18 and 20 GHz), this noise can therefore be particularly disturbing.

4. Imaging process

Using those scattered fields, the inversion procedure aims i) at detecting the presence of an inhomogeneity, ii) at localizing this inhomogeneity and at determining its maximum size and iii) at reconstruct-

ing its permittivity map. The procedure, described afterwards, is decomposed in two steps. First, we roughly determine the position of the target inside the measurement sphere delimited by the antennas positions and we estimate the minimum volume in which the target can be enclosed. This allows detecting the position and the size of the investigation domain. Then, to refine the inversion process to get quantitative information on the target, we reconstruct through an iterative procedure the permittivity map inside this pre-localized region.

We illustrate each step of this procedure with the results obtained from the scattered field measurements - calibrated and corrected from drift error - on the 6201 measured points and with a single polarization case. The two frequencies, 18 GHz and 20 GHz, are used. Indeed, the first step is realized at the lowest frequency and the second step uses the two frequencies in a frequency hopping approach, to obtain the results at 20 GHz.

4.1. Investigation domain

The inversion process is usually performed into a limited spatial domain called the investigation domain or the test domain. Even if some approaches exist to determine the investigation domain from the measured fields (see [*Bucci et al.*, 2003] for example), in most cases, this investigation domain is assumed to be known. Here, we propose to determine the position and the size of this domain directly from the measurements while taking into account the precision of the measurements.

4.1.1. Localization of the investigation domain

To localize the zone containing the target, we exploit the shape of the spatial spectrum of the "reduced scattered field", i.e., the scattered field multiplied by a phase term which depends on the position of the receiver with respect to the center of the target, as defined in [*Bucci et al.*, 1987]. We consider that the possible positions of this domain center $\mathbf{R}$ can be anywhere inside the sphere delimited by the transmitting antennas positions and the receiving antennas positions. For all the transmitting positions $\mathbf{s}$ and for each possible position $\mathbf{R}$, we can calculate the reduced measured scattered field $\mathbf{F}_s^m$ considering that the target can be enclosed in a sphere of radius a [*Bucci et al.*, 2006],

$$\mathbf{F}_s^m(\mathbf{R},\mathbf{r},\mathbf{s}) = \mathbf{E}_s^m(\mathbf{r},\mathbf{s})\, e^{jk\psi(\mathbf{r},\mathbf{R})} \qquad (1)$$

where $\mathbf{E}_s^m(\mathbf{r},\mathbf{s})$ is the scattered field measured at the position $\mathbf{r}$ for a source at the position $\mathbf{s}$, k is the background wave number and the phase factor is given by

$$\psi(\mathbf{r},\mathbf{R}) = \sqrt{d(\mathbf{r},\mathbf{R})^2 - a^2} - a\, cos^{-1}\left(\frac{a}{d(\mathbf{r},\mathbf{R})}\right) \qquad (2)$$

where $d(\mathbf{r},\mathbf{R})$ is the distance between the possible center position $\mathbf{R}$ and the receiver position $\mathbf{r}$. It can be noticed that to compute this term, we need to know the value of the sphere radius a enclosing the target, but we have found out that this value has limited influence on the determination of the sphere center $\mathbf{R}$ (for the following computations, we have set a equal to 10 cm). We then compute the Fourier transform of this reduced scattered field $\widehat{\mathbf{F}_s^m}$ along the receiver paths and we look at its spatial bandwidth $B_{\widehat{\mathbf{F}_s^m}}$:

$$B_{\widehat{\mathbf{F}_s^m}}(\mathbf{R},\mathbf{s}) = \left[\int \rho^2 |\widehat{\mathbf{F}_s^m}|^2 d\rho\right] / \left[\int |\widehat{\mathbf{F}_s^m}|^2 d\rho\right] \qquad (3)$$

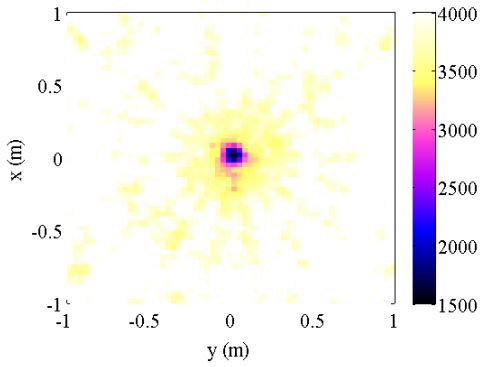

Figure 4. Map of $B^{sum}_{\widehat{\mathbf{F}_s^m}}$ when $R_z = 0$ cm

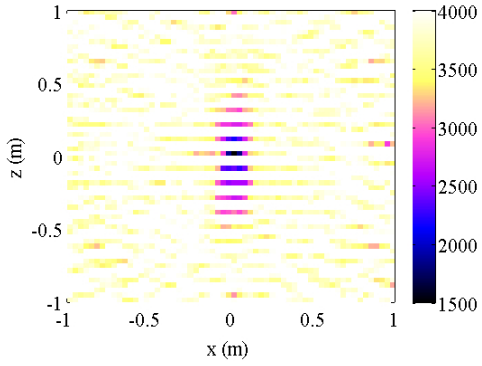

Figure 5. Map of $B^{sum}_{\widehat{\mathbf{F}_s^m}}$ when $R_y = 0$ cm

where ρ is the associated spatial Fourier coordinate for the receiver position. We then determine the center position $\mathbf{R}$ using the fact that the reduced scattered field must have a limited spatial bandwidth whatever the transmitting antenna position is. Thus, the position $\mathbf{R}^*$ is obtained when the following criterion reaches a minimum

$$B^{sum}_{\widehat{\mathbf{F}^m_s}}(\mathbf{R}) = \sum_{\mathbf{s}=1}^{N_s} \frac{B_{\widehat{\mathbf{F}^m_s}}(\mathbf{R},\mathbf{s})}{\sigma_{|\mathbf{F}^m_s|}(\mathbf{s})} \tag{4}$$

where N_s is the number of source positions and the weighting coefficients $\sigma_{|\mathbf{F}^m_s|}$ are directly estimated from the measurements. They enable to take into account the measurement accuracy which varies for each measurement point. For a given source position, these coefficients are corresponding to the mean on the receiver points of the measured noise standard deviations of the scattered field. In our case, we use the reciprocity principle to compute the 3D map of the quantity $B^{sum}_{\widehat{\mathbf{F}^m_s}}$ for various values of $\mathbf{R}$ in space, computed with a sampling of 1.5 cm (Figures 4, 5 and 6). From these figures, we can estimate that the criterion is minimum at the position $R^* = (0, 0, 0)$ cm. In particular, Figures 5 and 6 also enable to handle the lack of accuracy that we can expect with respect to the z axis, due to the limited number of measurements which are performed out of the azimuthal plane.

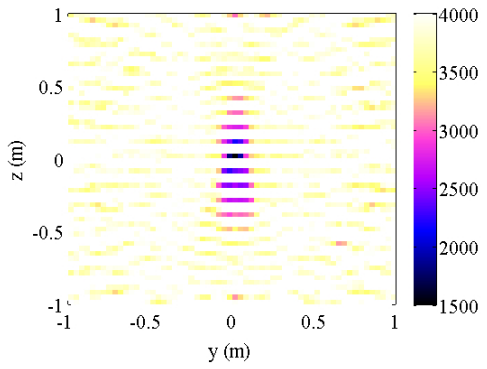

Figure 6. Map of $B^{sum}_{\widehat{\mathbf{F}^m_s}}$ when $R_x = 0$ cm

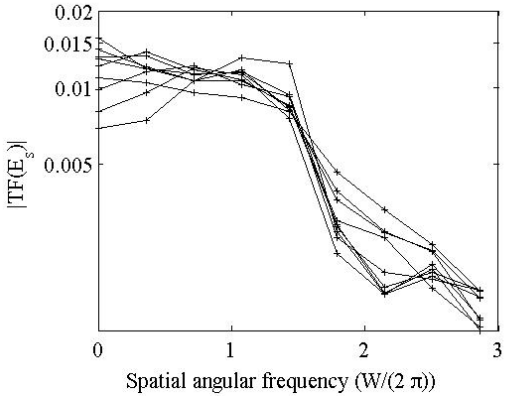

Figure 7. Plot of $\widehat{\mathbf{F}^m_s}$ computed along the vertical arch, for 9 different source positions, at 18 GHz.

4.1.2. Size of the investigation domain

Once the center of the sphere enclosing the target is estimated, we can then look at its minimum dimension. In our case, as the target is found at the center of the setup, which is also the center of the different circles where the receivers and the transmitters are moving on, the reduced scattered field is nothing but the scattered field multiplied by a constant phase term. This means that we can directly look at the spatial spectrum of the scattered field. As the bandwidth of this spectrum depends on the frequency and on the radius a of the minimum sphere enclosing the target [*Bucci et al.*, 1997], we can easily determine the radius of this minimum sphere. Using the reciprocity principle, we consider nine source positions placed with a constant angular step on the measurement circle in the xOy plane. For each of this source position, we examine the spectrum of the associated scattered field when measured along the vertical arch, while this arch is in the opposite position of the emitting antenna. In Figure 7, the experimental spectra are plotted. For each source position, the experimental spectrum presents a low-pass behavior which has a maximum spatial frequency of the order of 2.55. As this maximum spatial value depends on the dimension of the scatterer [*Bucci et al.*, 1987], we can conclude that the target can be enclosed into a sphere of radius $a = 4.3$ cm.

4.2. Iterative quantitative procedure

The previous subsection explained how to estimate the center position and the size of the investigation domain. In accordance with the estimated figures, we chose a cubic investigation domain centered at $\mathbf{R}^* = \mathbf{O}$ and with a size extent of 86 mm corresponding to $5.7\,\lambda$ at 20 GHz.

4.2.1. Principle

The permittivity map in this spatial domain is then deduced using an iterative inversion procedure. We have chosen to base our algorithm on a Bayesian

formulation [*Demoment et al.*, 2001], [*Baussard et al.*, 2001], [*Feron et al.*, 2005] to weigh the precision of the data. The probability to reconstruct this map depends directly on the random noise (nature and value) disturbing the measurements. The permittivity map solution is deduced from the *Maximum Likelihood* criterion and as we assume that there is no noise correlation from one measurement point to another, the cost function to minimize can be written as:

$$F_c^{(n)} = \sum_{s=1}^{N_s}\sum_{r=1}^{N_r} \frac{(Re[\mathbf{E}_s^m(\mathbf{s},\mathbf{r}) - \mathbf{E}_s^{(n)}(\mathbf{s},\mathbf{r})])^2}{\sigma_{Re}(\mathbf{s},\mathbf{r})^2} + \frac{(Im[\mathbf{E}_s^m(\mathbf{s},\mathbf{r}) - \mathbf{E}_s^{(n)}(\mathbf{s},\mathbf{r})])^2}{\sigma_{Im}(\mathbf{s},\mathbf{r})^2} \quad (5)$$

where N_s (resp. N_r) is the number of sources (resp. receivers), $\mathbf{E}_s^{(n)}$ is the simulated scattered field for the permittivity map estimated at the n-th iteration, σ_{Re} (resp. σ_{Im}) is the noise standard deviation on the real (resp. imaginary) part of the scattered field [*Eyraud et al.*, 2009]. Our minimization algorithm is based on a conjugated gradient procedure with standard Polak-Ribiere coefficients and a positivity constraint is used [*Kleinman et al.*, 1994]. The initial permittivity distribution is set to the background medium permittivity (more precisely, a small constant value is added to avoid the case where the gradients vanish due to the positive constraint expression). As the target is not dense, we expect this initial guess to be relatively close to the true solution. The investigation zone is discretized into cubic cells (with a lattice of $\lambda/10$ at 20 GHz) which corresponds to about 180 000 unknowns. The number of unknowns is clearly more important than the number of data, the possible false solutions due to the presence of local minima and the strategies to overcome this problem are carefully discussed in [*Isernia et al.*, 2001]. Here, we regularize our problem using the a-priori information on the noise and on physical a-priori constraints on the target permittivity map: positivity constraint and lossless condition.

The associated forward problem is performed in the frequency domain with a volume integral method [*Kong*, 2000]. The scattered field $\mathbf{E}_s$ on the receiver positions $r \in \Gamma$ is obtained with the observation equation:

$$\mathbf{E}_s(\mathbf{r}) = \int_\Omega \mathbf{G}_{or}(\mathbf{r},\mathbf{r}')\chi(\mathbf{r}')\mathbf{E}(\mathbf{r}')d\mathbf{r}' \quad (6)$$

where $\mathbf{G}_{or}$ is the free-space dyadic Green function between $\mathbf{r}' \in \Omega$ and $\mathbf{r} \in \Gamma$. χ is the permittivity contrast. The electric field $\mathbf{E}$ inside the zone Ω also satisfies the coupling equation, which fully takes into account the multiple scattering phenomena,

$$\mathbf{E}(\mathbf{r}') = \mathbf{E}_i(\mathbf{r}') + \int_\Omega \mathbf{G}_{oo}(\mathbf{r}',\mathbf{r}'')\chi(\mathbf{r}'')\mathbf{E}(\mathbf{r}'')d\mathbf{r}'' \quad (7)$$

where $\mathbf{E}_i$ is the incident field and $\mathbf{G}_{oo}$ is the free-space dyadic Green function. The field inside the imaging domain Ω is computed with a Bi-Conjugated Gradient Stabilized FFT method [*van der Vorst*,

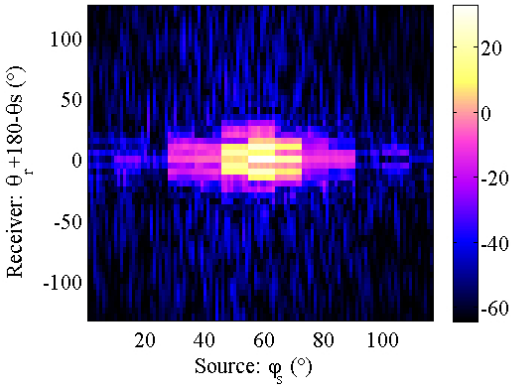

Figure 8. Random noise standard deviation on the real part of the scattered field, at 20 GHz. The plotted quantity is $20\,log(\sigma_{Re})$. For each source antenna position on the arch (ϕ_s angle), the target is illuminated with 9 incident directions (θ_s angle).

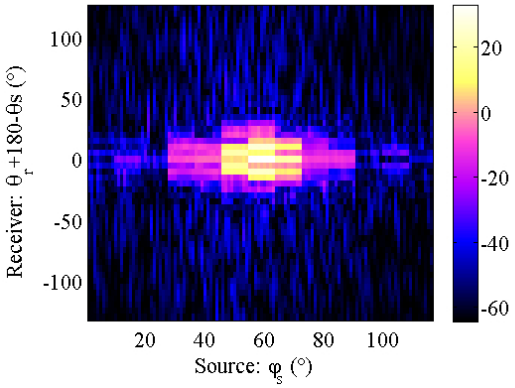

Figure 9. Random noise standard deviation on the imaginary part of the scattered field, at 20 GHz. The plotted quantity is $20\,log(\sigma_{Im})$. For each source antenna position on the arch (ϕ_s angle), the target is illuminated with 9 incident directions (θ_s angle).

2003] based on a 1D FFT to improve the calculation speed [*Barrowes et al.*, 2001]. The computation complexity is then of $O(NlogN)$ and the memory requirement is $O(N)$. More details on this algorithm can be found in [*Merchiers et al.*, 2010].

Considering the real random noise also allows defining an adequate stopping criterion in the inversion procedure. Indeed, the process is stopped when the cost function value becomes lower than 3σ, where σ is the mean of the measured noise standard deviation values. More details on this algorithm can be found in [*Eyraud et al.*, 2011].

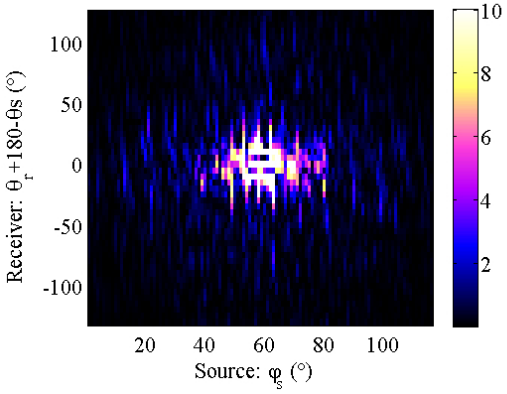

Figure 10. Behavior of the quadratic norm cost function according to the spatial measurement information at 20 GHz. The plotted quantity is Δf. For each source antenna position on the arch (ϕ_s angle), the target is illuminated with 9 incident directions (θ_s angle).

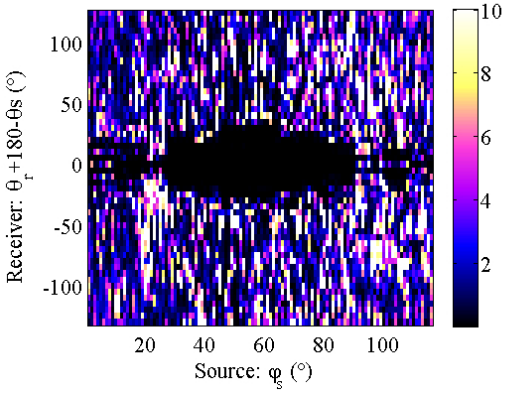

Figure 11. Behavior of the maximum likelihood cost function according to the spatial measurement information at 20 GHz. The plotted quantity is Δf. For each source antenna position on the arch (ϕ_s angle), the target is illuminated with 9 incident directions (θ_s angle).

4.2.2. Spatial behavior of the cost function

The minimized cost function (Eq. 5) is designed to incorporate the experimental random noise. It is therefore of interest to understand and/or verify the way the various weighting coefficients behave during the iterative process.

As it can be seen in Figures 8 and 9, the random noise is maximum in the forward scattering zone, meaning that the scattered field in this zone is not measured with the highest accuracy even if this is also the area where the scattered field magnitude is maximum. This behavior can be understood keeping in mind that the measurement is realized in two steps, i.e, firstly one measurement with the target

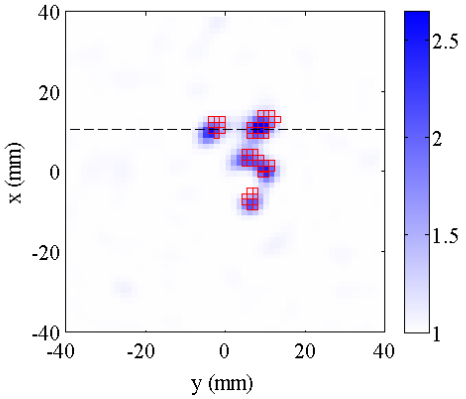

Figure 12. Reconstructed permittivity map plotted at $z = -22.4$ mm, obtained with the maximum likelihood cost function and a frequency hopping approach performed at 18 and 20 GHz The positions of the real spheres are over-plotted in red.

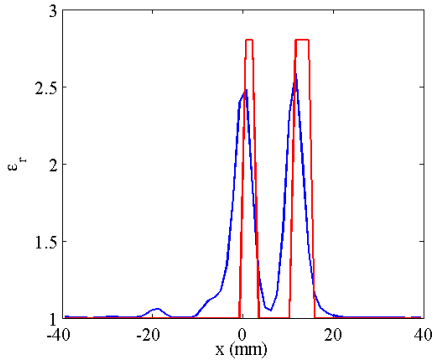

Figure 13. Profile of the reconstructed permittivity map (in blue), along the line plotted in Figure 12. The true profile is plotted in red.

(total field) is realized and secondly a measurement without the target (incident field) is performed and the random noise is in fact related to the measured fields which are the total and incident fields and not directly to the scattered field.

To see how this noise information is considered within the inversion algorithm, we compare the behavior of the cost function computed with the experimental standard deviations and the behavior of a classical quadratic norm cost function, where $\sigma_{Re} = \sigma_{Im} = 1$ for all the measurement points. To stress out the effects, we consider the variations of the error term between two iterations and for each measurement point. As the cost function can be written as

$$F_c^{(n)} = \sum_{s=1}^{N_s} \sum_{r=1}^{N_r} f^{(n)}(\mathbf{s}, \mathbf{r}),$$

the terms $\Delta f = |f^{(n+1)}(\mathbf{s}, \mathbf{r}) - f^{(n)}(\mathbf{s}, \mathbf{r})|$ are plotted for the last iteration (the behavior is similar for the other iterations) for the classical quadratic norm (Figure 10) and the maximum likelihood cost function (Figure 11).

We can see that the two behaviors are very different. Indeed, the quadratic norm cost function clearly favors a specific measurement zone during the reconstruction procedure, which is nothing but the forward scattering zone where the measurement accuracy has been detected to be the lowest in the present configuration. Looking now to the maximum likelihood cost function, we can see that this cost function exploits more efficiently the spatial diversity of the information content, i.e., each measurement point is balanced according to its own accuracy. As expected, the forward scattering zone is lowly taken into account.

4.2.3. Permittivity maps

The permittivity map of the investigation domain obtained after the quantitative iterative procedure is presented in the following. A cut along the horizontal plane at the altitude $z = -22.4\,\text{mm}$ is plotted in Figure 12. This figure enables to assess that the internal shape of the aggregate is correctly recovered, as the reconstructed spheres are very close to the real ones - represented in red in the figure. To evaluate quantitatively the global reconstruction, we have calculated the correlation between the reconstructed map and the real one considering all the voxels of the investigation zone. This criterion has been introduced in [*Eyraud et al.*, 2011] to quantify the similarities between the various maps. A high value of $Corr = 0.58$ is found here, which shows that the object is well reconstructed. In addition, the permittivity profile along the dotted line plotted in Figure 12, which is passing through the middle of two of the spheres, is provided in Figure 13. This figure shows a good agreement between the reconstructed permittivity value and the real one (the real profile is in red). Our procedure, which takes into account the multiple scattering effects and the uncertainties on the data, leads to a reconstructed permittivity map which is qualitatively and quantitatively pertinent, even for these small spheres which have a diameter equal to $\lambda/3$ at 20 GHz.

5. Conclusion

In this paper, we have proposed a complete imaging procedure from experimental fields. From (accurate and quantitative) measurements and without any a-priori knowledge on the scatterer, we have determined the position and the dimensions of the target and thus the investigation domain (first step of the inversion process) before retrieving its quantitative permittivity distribution (second step). We have moreover taken advantage at each step of the measurement accuracy that we have previously evaluated and carefully quantified. Indeed, for the first step, we have adopted a method based on the spatial spectrum properties of the (reduced) scattered field in which the measurements points are balanced with their own measurement accuracy. We have also shown that a Bayesian approach taking into account the random noise is well adapted to incorporate the spatial measurement sensitivity information into the quantitative procedure while performing the second inversion step. This imaging strategy leads to image presenting a clear super-resolution as it allows finding a target with a $5.7\,\lambda$ extent inside a measurement sphere diameter of $270\,\lambda$ and to retrieve quantitatively its detail of size $\lambda/3$, all of this being performed at 20 GHz. It can also be noticed that the reconstructed 3D quantitative permittivity map is precise even if the number of measurements is very weak compared to the number of possible reconstructed parameters, i.e, the number of reconstructed unknowns is about 30 time more important than the number of measurements. In future work, we plan to focus on the introduction in the inversion procedure of *a-priori* knowledge regarding the internal structure of the target, to fully exploit the capabili-

ties of the Bayesian approach to estimate the reconstructed parameter uncertainties, as well as measuring and imaging even more realistic targets.

Acknowledgments. We want to thank Rodolphe Vaillon, Bernard Lacroix and Olivier Merchiers from the CETHIL, Lyon, France for the design and the realization of the aggregate.

References

A. Abubakar and P. van den Berg, Iterative forward and inverse algorithms based on domain integral equation for three-dimensional electric and magnetic objects, *Journal Computational Physics*, *195*, 236–262, 2004.

B. Doudou and P. Sabouroux, EpsiMu, a toolkit for permittivity and permeability measurement in microwave domain at realtime of all materials: applications to solid and semisolid materials, *Microwave and Optical Technology Letters*, *59*, 2643–2648, 2010.

A. Brancaccio, V. Pascazio, R. Pierri, A quadratic model for inverse profiling: the one-dimensional case, *Journal of Electromagnetic Waves and Applications*, *9*, 673–696, 1997.

A. Baussard, D. Prémel and 0. Venard, A bayesian approach for solving inverse scattering from microwave laboratory-controlled data, *Inverse Problems*, *17*, 1659–1669, 2001.

B. E. Barrowes, L. F. Teixeira and J. A. Kong, Fast algorithm for matrix-vector multiply of asymmetric multilevel block-toeplitz matrices in 3-D scattering, *Microwave and Optical Technology Letters*, *31*, 28–32, 2001.

O. M. Bucci and G. Franceschetti, On the spatial bandwidth of scattered fields, *IEEE Trans. Antennas Propag*, *35*, 1445–1455, 1987.

O.M. Bucci and T. Isernia, Electromagnetic inverse scattering: retrievable information and measurement strategies, *Radio Science*, *32*, 2123–2137, 1997.

O.M. Bucci, A. Capozzoli and G. D'Elia, A novel approach to scatterers localization problem, *IEEE Trans. Antennas Propag*, *51*, 2079–2090, 2003.

O.M. Bucci, L. Crocco, M. D'Urso, and T. Isernia, Inverse scattering from phaseless measurements of the total field on open lines, *J Opt Soc Am A*, *23*, 2566–2577, 2006.

I. Catapano, L. Crocco, M. D'Urso and T. Isernia, 3D microwave imaging via preliminary support reconstruction: testing on the Fresnel 2008 database, *Inverse Problems*, *25*, 024002, 2009.

G. Demoment and J. Idier, Problèmes inverses : de l'expórientations à la modélisation: Approche bayésienne pour la résolution des problèmes inverses en imagerie, *M. Bonnet ed., Observatoire francais des techniques avancées, Paris*, 59–77, 2001.

C. Eyraud, J.-M. Geffrin, A. Litman, P. Sabouroux and H. Giovannini, Drift correction for scattering measurements, *Applied Physics Letters*, *89*, 244104, 2006.

C. Eyraud, J.-M. Geffrin, P. Sabouroux, P. Chaumet, H. Tortel, H. Giovannini and A. Litman, Validation of a 3D bistatic microwave scattering measurement setup, *Radio Science*, *43*, RS4018, 2008.

C. Eyraud, A. Litman, A. Hérique and W. Kofman, Microwave imaging from experimental data within a Bayesian framework with realistic random noise, *Inverse Problems*, *26*, 024005, 2009.

C. Eyraud and J.-M. Geffrin and A. Litman, 3D-aggregate quantitative imaging: experimental results and polarization effects, *IEEE Trans. Antennas Propag*, *59*, 1237 - 1244, 2011.

O. Féron, B. Duchêne and A Mohammad-Djafari, Microwave imaging of inhomogeneous objects made of a finite number of dielectric and conductive materials from experimental data, *Inverse Problems*, *21*, S95–S115, 2005.

Fresnel forward problem datasets: see the following link http://www.fresnel.fr/3Ddirect/database.php.

T. Isernia, V. Pascazio and R. Pierri, A non-linear estimation method in tomographic imaging, *IEEE Trans. Geoscience and Remote Sensing*, *35*, 910–923, 1997.

T. Isernia, V. Pascazio and R. Pierri, On the local mimima in a tomographic imaging technique, *IEEE Trans. Geoscience and Remote Sensing*, *39*, 1596–1607, 2001.

L. Garnero, A. Franchois, J.-P. Hugonin, C. Pichot, N. Joachimowicz, Microwave imaging-complex permittivity reconstruction-by simulated annealing , *IEEE Trans. Microwave Theory and Techniques*, *39*, 1801 - 1807, 1991.

J.-M. Geffrin, P. Sabouroux and C. Eyraud, Free space experimental scattering database continuation: Experimental setup and measurement precision, *Inverse Problems*, *21*, S117–S130, 2005.

J.-M. Geffrin, C. Eyraud, A. Litman and P. Sabouroux, Optimization of a Bistatic Microwave Scattering Measurement Setup:From High to Low Scattering Targets, *Radio Science*, *44*, RS003837, 2009.

J.-M. Geffrin and P. Sabouroux, Fresnel database continuation: Experimental setup and improvements for 3d scattering measurements, *Inverse Problems*, *25*, 024001, 2009.

R. E. Kleinman and P. M. van den Berg, An extended modified gradient technique for profile inversion, *Radio Science*, *28*, 877–884, 1993.

R. E. Kleinman and P. M. van den Berg, Two-dimensional location and shape reconstruction, *Radio Science*, *29*, 1157–1169, 1994.

J. A. Kong, Electromagnetic wave theory, *EMW*, 2000.

A. Litman and L. Crocco, Guest editor introduction, *Inverse Problems*, *25*, 020201, 2009.

A. Litman H.Tortel and M. Guillaume Resolution-improved microwave tomography by means of hyperspectral analysis tools, *13th International Conference on Ground Penetrating Radar (GPR), Lecce, Italy*, 2010.

O. Merchiers, J.-M. Geffrin, R. Vaillon, P. Sabouroux and B. Lacroix, Microwave analog to light scattering measurements on a fully characterized complex aggregate, *Applied Physics Letters*, *94*, 181107, 2009.

O. Merchiers, C. Eyraud, J.-M. Geffrin, R. Vaillon, B. Stout, P. Sabouroux and B. Lacroix, Microwave measurements of the full amplitude scattering matrix of a complex aggregate: a database for the assessment of light scattering codes, *Optics Express*, *18*, 121191, 2010.

P. Sabouroux, J.-M. Geffrin and C. Eyraud, An original microwave near-field/ far-field spherical setup: Applications to antennas and scattered field measurements, *Proc. Antenna Measurement Tech. Assoc. Symp.*, *Newport, RI, USA*, 292–296.

S. Semenov, A. Bulyshev, A. Souvorov, A. Nazarov, Y. Sizov, R. Svenson, V. Posukh, A. Pavlovsky, P. Repin, and G. Tatsis, Three-dimensional microwave tomography: experimental imaging of phantoms and biological objects, *IEEE Trans. Microwave Theory Techniques*, *48*, 1071–1074, 2000.

R.K. Snieder and J. Trampert, A simple processing approach for holographic rascan data, *Inverse problems in geophysics*, In: Wirgin, A. (Ed.), Wavefield Inversion. Springer, New York, pp. 119190, 1999.

F. Soldovieri, A simple processing approach for holographic rascan data, *Progress In Electromagnetics Research*, *107*, 315-330, 2010.

F. Soldovieri, F. Ahmad and R. Solimene Validation of Microwave Tomographic Inverse Scattering Approach via Through-the-Wall Experiments in Semicontrolled Conditions, *IEEE Geosci. Remote Sens. Letters*, *8*, 123-127, 2011.

A.G. Tijhuis, K. Belkebir, A. Litman and B.P. de Hon, Multiple-frequency distorted-wave Born approach to 2D inverse profiling, *Inverse Problems*, *17*, 1635–1644, 2001.

P. M. van den Berg, M. G. Coté and R. E. Kleinman, Blind shape reconstruction from experimental data, *IEEE Trans. Antennas Propag*, *43*, 1389–1396, 1995.

H. A. van der Vorst, Iterative Krylov Methods for Large Linear Systems, *Cambridge University Press*, 2003.

J. de Zaeytijd, A. Franchois, and J.-M. Geffrin, A new value picking regularization strategy-application to the 3-d electromagnetic inverse scattering problems, *IEEE Trans. Antennas and Propagation*, *57*, 1133–1149, 2009.

A.A. Zigliavsky, Theory of global random search, *Springer Verlag*, 1991.

Christelle Eyraud, Jean-Michel Geffrin, Amélie Litman, Jean-Pierre Spinelli, Institut Fresnel, Campus Universitaire de St Jérôme, 13397 Marseille cedex 20, France. (christelle.eyraud@fresnel.fr)

(Received _____.)